12.7 THE NCEP WRF CORE

Zavisa I. Janjic*
National Centers for Environmental Prediction, Camp Springs, Maryland

1. INTRODUCTION

With constantly increasing horizontal resolution, numerical weather prediction models are approaching the limits of validity for the hydrostatic approximation. Although considerable experience with nonhydrostatic models has been accumulated on the scales of convective clouds and storms, numerical weather prediction (NWP) deals with motions on a much wider range of temporal and spatial scales. Difficulties that may not be significant, or may go unnoticed at small scales, may become important in NWP applications. For example, an erratic gain or loss of mass would be hard to tolerate in an operational environment. Problems may also arise with spurious motions generated in the upper levels by the nonhydrostatic dynamics and numerics. Forcing the variables in the top model layers toward a steady state in response to this problem is inadequate for NWP, and, on the other hand, specifying time dependent computational top boundary conditions would limit the ability of the nested model to produce more accurate forecasts than the parent model.

Having in mind these considerations, a novel approach (Janjic et al., 2001; Janjic, 2003) has been applied in the NCEP Nonhydrostatic Meso Model (NMM) that was developed within the Weather Research and Forecasting (WRF) initiative. Namely, instead of extending cloud models to larger spatial and temporal scales, the hydrostatic approximation is relaxed in a hydrostatic NWP model using advanced numerics and a vertical coordinate based on hydrostatic pressure. In this way, the applicability of the model is extended to nonhydrostatic motions and at the same time the favorable features of the hydrostatic formulation of the numerical algorithms have been preserved within the range of validity of the hydrostatic approximation.

With this approach, the nonhydrostatic equations are split into two parts: (a) the part that corresponds to the hydrostatic system, except for corrections due to the vertical acceleration; and (b) the part that allows computation of the corrections appearing in the first system. The separation of the nonhydrostatic contributions shows in a transparent way where, how and to what extent the hydrostatic approximation affects the equations. The described procedure does not require any linearization or additional approximation.

*Corresponding author address: Zavisa I. Janjic, National Centers for Environmental Prediction, 5200 Auth Rd., Camp Springs, MD 20746; e-mail: Zavisa.Janjic@noaa.gov

2. MODEL EQUATIONS

For simplicity, as a representative of mass based vertical coordinates, consider the sigma coordinate

$$\sigma = \frac{(\pi - \pi_t)}{\mu}, \tag{2.1}$$

where π is the hydrostatic pressure, and μ represents the difference in hydrostatic pressure between the base and the top of the model column

$$\mu = \pi_s - \pi_t . \tag{2.2}$$

Here, π_s and π_t stand for the hydrostatic pressures at the surface and at the top of the model atmosphere. Then, the equations governing a dry, inviscid and adiabatic nonhydrostatic atmosphere are (Janjic et al., 2001; Janjic 2003)

$$\frac{d\mathbf{v}}{dt} = -(1+\varepsilon)\nabla_\sigma \Phi - \alpha \nabla_\sigma p + f\mathbf{k}\times\mathbf{v}, \tag{2.3}$$

$$\frac{\partial T}{\partial t} = -\mathbf{v}\bullet\nabla_\sigma T - \dot\sigma\frac{\partial T}{\partial \sigma} + \frac{\alpha}{c_p}\left(\frac{\partial p}{\partial t} + \mathbf{v}\bullet\nabla_\sigma p + \dot\sigma\frac{\partial p}{\partial\sigma}\right), \tag{2.4}$$

$$\sigma\frac{\partial \mu}{\partial t} = -\int_0^\sigma \left[\nabla_\sigma\cdot(\mu\mathbf{v}) + \frac{\partial(\mu\dot\sigma)}{\partial\sigma}\right]d\sigma', \tag{2.5}$$

$$p\alpha = RT, \tag{2.6}$$

$$\frac{1}{\mu}\frac{\partial\Phi}{\partial\sigma} = -\alpha, \tag{2.7}$$

$$w = \frac{1}{g}\left(\frac{\partial \Phi}{\partial t} + \mathbf{v} \bullet \nabla_\sigma \Phi + \dot{\sigma}\frac{\partial \Phi}{\partial \sigma}\right), \qquad (2.8)$$

$$\varepsilon \equiv \frac{1}{g}\frac{dw}{dt}, \qquad (2.9)$$

$$\frac{\partial p}{\partial \pi} = 1 + \varepsilon\,. \qquad (2.10)$$

Here, in the order of appearance, $\mathbf{v}$ is the horizontal wind vector, p is the actual, nonhydrostatic pressure, R is the gas constant for dry air, T is temperature and Φ is geopotential. The other symbols used have either their usual meaning, or their meaning is self-evident. Note that Φ, w, and ε are not independent variables.

The parameter ε is the central point of the extended, nonhydrostatic dynamics. As can be readily verified, if ε is zero, the considered equations reduce to the familiar, hydrostatic system of equations. On the synoptic scale, ε is small and approaches the computer round–off error. However, in the case of vigorous convective storms, or strong vertical accelerations in the flows over steep obstacles, ε can reach 10^{-3}. For this value of ε the nonhydrostatic deviation of pressure can reach 100 *Pa*. Bearing in mind that the typical synoptic scale horizontal pressure gradient is on the order of 100 *Pa* over 100 *km*, this suggests that significant local nonhydrostatic pressure gradients and associated circulations may develop at small scales. Nevertheless, ε remains much smaller than 1 in atmospheric flows, and, therefore, the nonhydrostatic effects are on a higher order of magnitude. An important consequence of this situation for discretization is that a high accuracy of computation of ε does not appear to be of paramount importance, since the computational errors are of even higher order than ε.

The method of solving of the considered system of nonhydrostatic equations is presented in detail in Janjic et al. (2001). Further details and updates are presented in Janjic (2003). Here, only the basic principles of the discretization will be reviewed and the reader is referred to the quoted papers for more details.

3. CLASSICAL NONHYDROSTATIC SOLUTIONS

In order to test the validity of the approach in the limit of highly nonhydrostatic flows, a two-dimensional model in the vertical plane was developed and run in a series of classical nonhydrostatic tests (Janjic et al., 2001). As is usual at these scales, the Coriolis force was neglected. Some of the results of Janjic et al. (2001) obtained in the cold and warm bubble tests will be reproduced here as examples. For more details about these and other tests, the reader is referred to Janjic et al. (2001).

Following Straka et al. (1993), in a neutrally stratified atmosphere with the potential temperature of $300^0 K$, an initial cold disturbance of the form

$$T(x,z) = \overline{T}(x,z) - 15\cos^2\left[\frac{\pi}{2}\sqrt{\left(\frac{x-x_c}{x_t}\right)^2 + \left(\frac{z-z_c}{z_t}\right)^2}\right],$$

$$if \quad \sqrt{\left(\frac{x-x_c}{x_t}\right)^2 + \left(\frac{z-z_c}{z_t}\right)^2} \le 1$$

was introduced, where

$$x_c = 0\ m,\ z_c = 3000\,m,$$
$$x_t = 4000\ m,\ z_t = 2000\,m.$$

The integration domain extended 40 *km* in the x direction, and the free surface was located at 442 *hPa*, or about 6400 *m*. The center of the initial disturbance was in the middle of the domain in the x direction, 20 *km* away from either of the lateral boundaries. As in the main test in the Straka et al. (1993) study, the horizontal resolution was 100 *m*, and the vertical resolution was 100 *m* on the average. The time step was 0.3 *s*.

The potential temperatures after 300 *s*, 600 *s* and 900 *s* are displayed in Fig. 1. The area shown in the

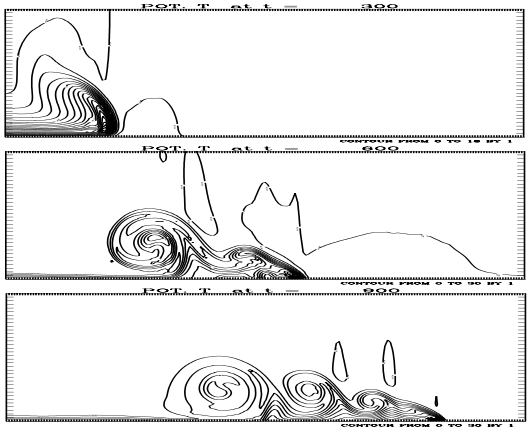

Fig. 1. The cold bubble test. Initial potential temperature and the potential temperatures after 300 *s*, 600 *s* and 900 *s* in the right hand part of the integration domain extending from the center to 19200 m, and from the surface to 4600 m. The grid size is $\Delta z \approx \Delta x = 100$ m and $\Delta t = 0.3$ s. The contour interval is 1^0 K.

figure extends from the center of the domain to 19200 *m* to the right, and from the surface to 4600 *m*. The contour interval is 1^0 K. Comparison of the results obtained in this test (Janjic et al., 2001) with the Straka et al. (1993) converged reference solution reveals good quantitative and qualitative agreement.

The hydrostatic dynamics was unable to reproduce the results shown in Fig. 1 (Janjic et al., 2001). The hydrostatic solution was computationally unstable unless the lateral diffusion was increased by an order of magnitude. In that case, however, only very crude, qualitative resemblance to the nonhydrostatic solution was preserved.

The warm bubble test was designed following Gallus and Rancic (1996). In a neutral atmosphere with the potential temperature of $300^0 K$, an initial disturbance of the potential temperature

$$\theta(x,z) = \bar{\theta}(x,z) + 6.6\cos^2\left[\frac{\pi}{2}\sqrt{\left(\frac{x-x_c}{x_t}\right)^2+\left(\frac{z-z_c}{z_t}\right)^2}\right], \quad if \quad \sqrt{\left(\frac{x-x_c}{x_t}\right)^2+\left(\frac{z-z_c}{z_t}\right)^2} \le 1$$

was introduced, where

$$x_c = 0 \ m, \ z_c = 2750\, m,$$
$$x_t = 2500 \ m, \ z_t = 2500\, m.$$

The integration domain extended 20 *km* in the x direction. The free surface was located at 135 *hPa*, or at about 13500 *m*. The center of the initial disturbance was in the middle of the domain in the x direction, i.e., 10 *km* away from either of the lateral boundaries. The horizontal resolution was 100 *m*, and the vertical resolution was 100 *m* on the average. The time step with this spatial resolution was 0.3 *s*, as before.

The potential temperature deviations after 360 *s*, 540 *s*, 720 *s* and 900 *s* are presented in Fig. 2. The area shown extends 16 *km* along the x axis, and from 1000 *m* to 13200 *m* along the z axis. The contour interval is $1^0 K$. The rate of ascent and the intensity of the disturbance agree with those reported elsewhere.

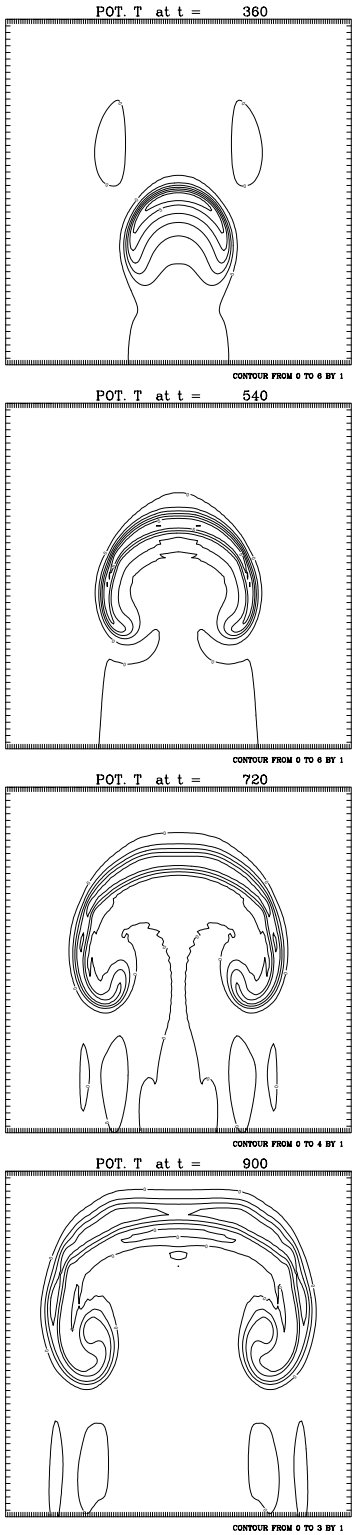

Fig. 2. The potential temperature deviation after 360 *s*, 540 *s*, 720 *s* and 900 *s* (from top to bottom) in the warm bubble test. The area shown extends 16 *km* along the x axis, and from 0 *m* to 13200 *m* along the z axis. The contour interval is $1^0 K$.

4. HORIZONTAL GRID AND HORIZONTAL COORDINATES

The choice of the horizontal grid is one of the first decisions that needs to be made in the process of designing a numerical model of the atmosphere.

Winninghoff (1968) and Arakawa and Lamb (1977) examined the frequencies of gravity-inertia waves obtained using second-order centered differences on various types of rectangular horizontal grids. According to these studies, compared to other grids considered, generally better agreement with the exact frequencies were obtained on the staggered grid C, and on the semi-staggered grid B (or E) shown in Fig. 3. The

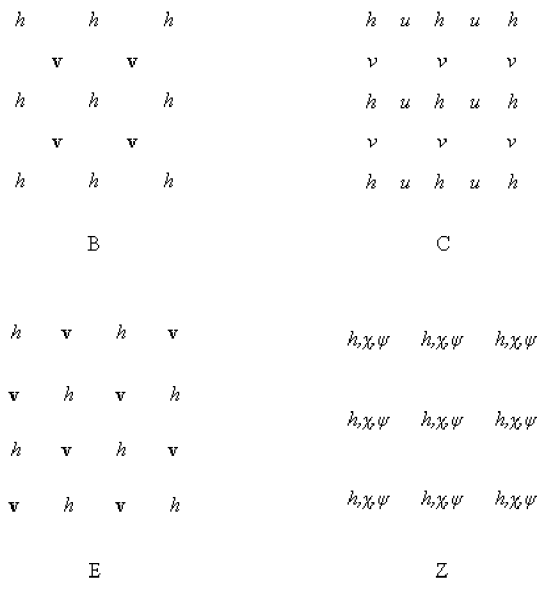

Fig. 3. The staggered grid C and the semi-staggered grids B, E and Z.

symbol h in the figure denotes the mass point variables, while the horizontal velocity vector and the velocity components are denoted, respectively, by $\mathbf{v}$, u and v. However, the staggered grid and the semi-staggered grids are not without problems, either. The problems on the staggered grid arise due to the averaging of the velocity components in the Coriolis force terms. On the other hand, in order to illustrate the problems on the semi-staggered grids, consider the shallow water equations

$$\frac{\partial u}{\partial t} = -g\frac{\partial h}{\partial x} + fv\,,\ \ \frac{\partial v}{\partial t} = -g\frac{\partial h}{\partial y} - fu\,,$$
$$\frac{\partial h}{\partial t} = -H\left(\frac{\partial u}{\partial x} + \frac{\partial v}{\partial y}\right). \qquad (4.1)$$

Here, u and v are the velocity components, h is the height of the free surface, g is gravity, f is the Coriolis parameter assumed to be constant, and H is the mean depth of the fluid. The other symbols used have their usual meaning. The system (4.1) discretized in the most straightforward way, e.g., on the B grid, has the form

$$\frac{\partial u}{\partial t} = -g\delta_x \bar{h}^{\,y} + fv\,,\ \ \frac{\partial v}{\partial t} = -g\delta_y \bar{h}^{\,x} - fu\,,$$
$$\frac{\partial h}{\partial t} = -H(\delta_x \bar{u}^{\,y} + \delta_y \bar{v}^{\,x})\,. \qquad (4.2)$$

In (4.2), the symbol δ and the overbar, respectively, represent the simplest two-point centered differencing and averaging operators applied in the direction indicated by the accompanying subscript or superscript. Following Janjic (1984), the velocity components on the B grid may be written in terms of the velocity potential χ and the stream function ψ in the form

$$u = \delta_x \bar{\chi}^{\,y} - \delta_y \bar{\psi}^{\,x}\,,\ v = \delta_y \bar{\chi}^{\,x} + \delta_x \bar{\psi}^{\,y}\,. \qquad (4.3)$$

Then, after substituting the expressions (4.3) into the system (4.2), and rearranging the terms, one obtains

$$\frac{\partial \chi}{\partial t} = -gh + f\psi\,,\ \frac{\partial \psi}{\partial t} = -f\chi\,,$$
$$\frac{\partial h}{\partial t} = -H(\delta_{xx}\bar{\chi}^{\,yy} + \delta_{yy}\bar{\chi}^{\,xx})\,, \qquad (4.4)$$

where repeated subscripts and superscripts indicate repeated applications of the accompanying operators. As can be seen from (4.4), the only possible reason for the B grid problems is the insufficiently accurate computation of the Laplacian due to the averaging of the derivatives of the velocity potential χ in the continuity equation. An inspection of the finite difference equations (4.4) reveals that they are defined on a nonstaggered grid, carrying all three variables χ, ψ and h at each grid point (Janjic 1984). This type of grid is also shown in Fig. 3. It was named Z grid by Randall (1994). Thus, the B grid, together with the definitions (4.3), is equivalent to the Z grid. However, there is an important difference between the B and Z grid simulations of the gravity-inertia wave propagation. On the Z grid, the continuity equation can be written in the form

$$\frac{\partial h}{\partial t} = -H(\delta_{xx}\chi + \delta_{yy}\chi)\,, \qquad (4.5)$$

without the averaging in the divergence term that was responsible for the B grid problems. However, an application of the Z grid in the case of more complex equations would require costly conversions between the

velocity components and the velocity potential and the stream function. A more complete comparison of the properties of the remaining two possibilities, the staggered grid C and the semi-staggered grids B and E can be found, e.g., in Janjic and Mesinger (1984, 1989). These considerations, however, do not give a decisive advantage to either of the two choices. The problems on the semi-staggered grids B and E are restricted mainly to the shortest waves, while in the case of slow internal modes and/or weak stability, the C grid may develop problems over the entire range of admissible wave numbers (Arakawa and Lamb, 1977). In addition, there is an effective technique for filtering the low frequency, short-wave noise resulting from inaccurate computation of the divergence term on the semi-staggered grids (Janjic, 1979). More sophisticated, nondissipative methods ("deaveraging" and "isotropisation") for dealing with the problem also have been proposed (Janjic et al., 1998), leading to dramatic improvements in the finite-difference frequencies of short gravity-inertia waves on the semi-staggered grids.

The results discussed so far are relevant for classical synoptic scale models. In order to address the question of the horizontal grid choice as the mesoscales are approached, the linearized anelastic nonhydrostatic system is a better starting point than the linearized shallow water equations (4.1) (communicated by Klemp, 1997; Janjic, 2003).

As before, the problems on the B grid are mainly due to averaging within the divergence term, and on the C grid are mainly due to the averaging of the Coriolis force. For example, if the ratio between the horizontal grid size and the vertical grid size is 30, $f = 0.0001$, the Brunt-Vaisala frequency is $N = 0.0001$, and the wavelength in the vertical is 32 grid intervals, the true relative frequency v / f and the relative frequency on the B grid are both equal to unity throughout the admissible wave number range. On the other hand, as can be seen from Fig. 4, with the same values of the parameters the relative frequency on the C grid is not a constant. This leads to a nonzero group velocity throughout the admissible wave-number range, including the longest waves. For more details concerning this example, the reader is again referred to Janjic (2003).

On the other hand, the example shown in Fig. 5 indicates how bad the problem can be on the B grid. The two 24 hour sea level pressure forecasts shown in the figure were computed using 30 *km* horizontal resolution and very light dissipation. The contour interval was set to 1 *hPa* in order to emphasize any noise that might develop. The forecast in the upper panel was obtained by doing nothing to alleviate the B grid

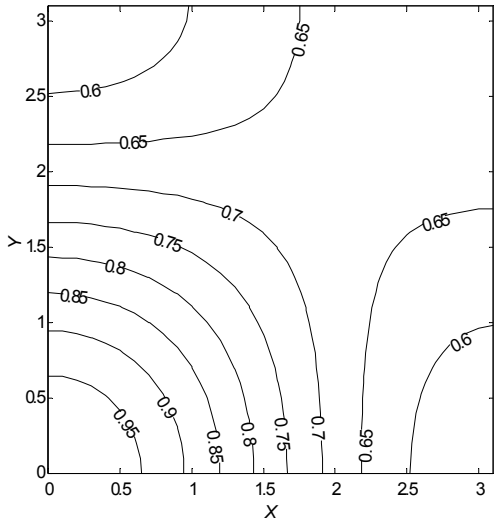

Fig. 4. The ratio v_C / f as a function of wave number.

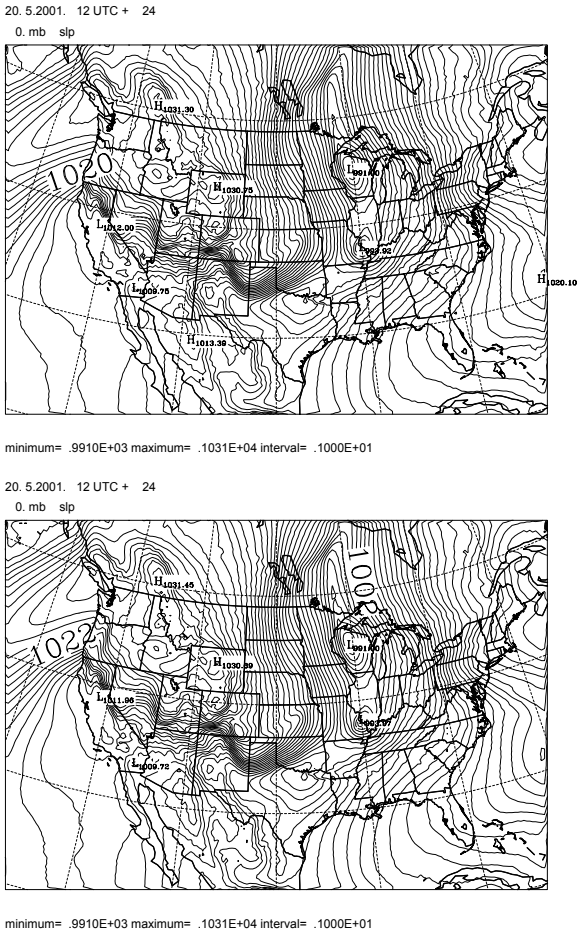

Fig. 5. Examples of 24 hour forecasts of the sea level pressure on the B grid without any control of the grid separation problem (upper panel) and with deaveraging (lower panel). The contour interval is 1 *hPa*.

problem, while the forecast in the lower panel was obtained using well converged “deaveraging” (Janjic et al., 1998), which substantially improves the frequencies of gravity-inertia waves on the B grid. As can be seen by comparing the forecasts in the upper panel and in the lower panel, the presence of the problem cannot be visually detected. The forecast in the upper panel generally is not noisier than the forecast in the lower panel. This result appears to be in conflict with an earlier result (Janjic, 1979). However, in the earlier test the horizontal resolution was 160 *km*, so the advection had a lesser effect in providing communication between the grid points than in the current test with the 30 *km* resolution.

Since the problems on the semi-staggered grid B are restricted to the shortest resolvable scales, and they are less sensitive to the stability and choice of vertical and horizontal grid sizes, preference was given to the semi-staggered grids. For historical reasons, the E grid is used in the initial version of the NCEP Nonhydrostatic Meso model (NMM), although a B grid version with identical properties also exists (Janjic, 2003).

The longitude-latitude coordinates are rotated in the model in such a way that the coordinate origin is located in the middle of the integration domain. In this way, the reduction in longitudinal grid-size is minimized as the southern and the northern boundaries of the integration domain are approached, and, therefore, longer time steps can be used.

5. VERTICAL COORDINATE AND VERTICAL STAGGERING

By far the most widely used method for representing topography are terrain following coordinates such as the sigma coordinate (Phillips, 1957), or its extensions such as the hybrid sigma-pressure coordinate of Arakawa and Lamb (1977), or the hybrid eta coordinate of Simons and Burridge (1981). A rare exception has been the step-mountain blocking used in the NCEP Meso (Eta) model. Originally proposed by Bryan (1969), and subsequently widely used in oceanography, this technique was implemented in an atmospheric model by Mesinger et al. (1988). Yet another possibility for the representation of topography is the shaved cell method (e.g. Adcroft et al. 1997). Steppeler et al. (2002) reported a successful application of this approach in the Local Model (LM) of the German Weather Service.

The advantage of the step-like mountain representation is that the coordinate surfaces are quasi-horizontal. This, however, is not without consequences. For example, internal discontinuities are introduced at the vertical sides of the steps that replace mountain slopes, and lateral boundary conditions are required at these discontinuities. The formal accuracy of the finite-differences at points next to the internal boundaries is reduced to the first order. In addition, if no slip boundary conditions are used in order to preserve the major favorable features of the finite-differencing schemes (Janjic, 1977, 1979, 1984), a nonphysical sink of momentum is introduced. Yet another problem is the representation of physical processes in the surface layer and the planetary boundary layer (PBL). If one wants to represent these processes in a reasonably uniform way throughout the integration domain, including both low-lying and elevated terrain, an approximately equidistant spacing of the vertical levels is required in the lowest few kilometers of the atmosphere. However, the vertical resolution needed in order to achieve this goal is still too high. In addition, several recent studies (Adcroft et al, 1997; Gallus, 2000; Gallus and Klemp, 2000; Janjic and DiMego, 2001; Gavrilov, 2002) indicate that more problems should be expected at higher resolutions.

The shaved cell approach has problems associated with complex lower and internal boundary conditions. In addition, as with the step-mountains, vertical resolution is reduced over elevated terrain, which poses additional problems for physical parameterizations.

Thus, despite of all its imperfections, the terrain-following hybrid pressure-sigma vertical coordinate (Arakawa and Lamb, 1977) has been chosen as the best compromise (Janjic, 2003). With the hybrid coordinate, coordinate surfaces are flat above and away from the mountains. In the vicinity of mountains the hybrid coordinate has increased vertical resolution, and the equations are continuous, without the computational internal boundary conditions. Since hydrostatic pressure is currently used as the vertical coordinate above 400 *hPa*, possible inaccuracies due to the sloping coordinate surfaces are restricted to only the lower half of the mass of the atmosphere. Note that, generally, the largest errors in the sigma coordinate occur in the stratosphere. Thus, with the hybrid coordinate, the most serious problems associated with sloping sigma surfaces are eliminated. In addition, the increased resolution presumably acts in the direction of reducing computational inaccuracies, and certainly improves the representation of the vertical PBL structure over elevated terrain.

The usual, Lorenz vertical staggering of the variables is used in the vertical (Janjic, 1977). The geopotential and nonhydrostatic pressure are defined at the interfaces of the layers, while all three velocity components and temperature are carried in the middle

layers of the model. The vertical velocity is defined at the E grid mass points.

6. SPATIAL DISCRETIZATION

Conservation of major integral properties such as energy and enstrophy has been the basic philosophy of the discretization that can be tracked back to the paper by Janjic (1977). Since then, however, the numerical schemes used in the model have been further refined. Perhaps the most significant upgrade was the introduction of new schemes for calculating the contribution of nonlinear advection terms and horizontal divergence operators (Janjic, 1984). Properties of the momentum advection scheme were further investigated by Gavrilov and Janjic (1989). In the current model formulation, all divergence operators are computed using the fluxes between each point and its eight nearest neighbors. This "isotropic" divergence operator is used in the Arakawa Jacobian, and also in the hydrostatic continuity equation in order to compute the divergence of mass.

In the case of rotational flow and cyclic boundary conditions, the scheme for horizontal advection of momentum on the E grid conserves the following properties:

- Enstrophy as defined on the staggred grid C (i.e. using the most accurate second-order approximation of the Laplacian in order to compute vorticity),

$$\sum_{i,j}(\delta_{x'x'}\psi+\delta_{y'y'}\psi)^2\,\Delta A\,, \qquad (6.1)$$

- Rotational kinetic energy as defined on the staggered grid C,

$$\sum_{i,j}\frac{1}{2}(\delta_{y'}\psi)^2\,\Delta A+\sum_{i,j}\frac{1}{2}(\delta_{x'}\psi)^2\,\Delta A\,, \qquad (6.2)$$

- Rotational momentum as defined on the staggered grid C,
- Rotational kinetic energy as defined on the semi-staggered grid E,

$$\sum_{i,j}\frac{1}{2}[\delta_y\psi^2+\delta_x\psi^2]\Delta A\,, \qquad (6.3)$$

- Rotational momentum as defined on the semi-staggered grid E.

The Z grid equivalent of the E grid used to define the quantities (6.1)-(6.3) is shown in Fig. 6 together with the orientation of the coordinate axes x,y and x',y'

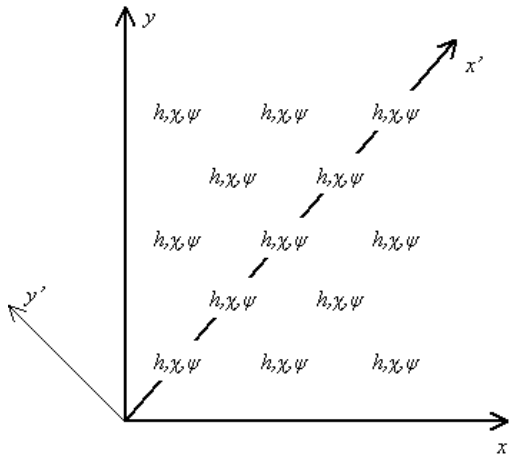

Fig. 6. The Z grid equivalent of the E grid. Orientations of the coordinate axes x,y and x',y' are indicated.

appearing in (5.1)-(5.3). As before, φ and ψ are the velocity potential and the stream function, respectively, and h stands for mass point variables. The symbol ΔA denotes the area of the grid boxes, and the summation sign with the subscripts i,j represents the horizontal summation.

In the case of general flow, the scheme conserves:

- Kinetic energy as defined on the semi-staggered grid E

$$\sum\frac{1}{2}[(\delta_x\varphi-\delta_y\psi)^2+(\delta_y\varphi+\delta_x\psi)^2]\Delta V\,, \qquad (6.4)$$

- Momentum as defined on the semi-staggered grid E.

In (6.4), the summation sign indicates summation over all grid points, and the symbol ΔV denotes the grid box volume in hydrostatic vertical coordinates.

The scheme for horizontal advection of temperature also conserves the first and the second moments of temperature. Finally, in the hydrostatic limit, when dw/dt tends to zero, the exact cancellation is achieved between the contributions of the pressure gradient force to the kinetic energy generation, and the $\omega\alpha$ term of the thermodynamic equation, which guarantees consistent transformations between kinetic and potential energy, and the conservation of total energy. Note that

the treatment of the $\omega\alpha$ term implies exact cancellation of the contribution from advection of pressure in the thermodynamic equation and the contribution from the second term of pressure gradient force in the momentum equations. The relevant finite-difference schemes were presented in Janjic (1977), and their generalizations for the "isotropic", 8-flux divergence operators were discussed in Janjic (1984) and further documented, e.g., in Mesinger et al. (1988).

Exact energy conservation is not currently required in the case of fully nonhydrostatic equations. In this case, the terms involving $\varepsilon = (dw/dt)/g$ are of a higher order than quadratic, and $\varepsilon = (dw/dt)/g$ is small compared to unity in the weakly nonhydrostatic flows that can be expected in NWP applications. On the other hand, at the scales and in flow regimes where the contribution of $\varepsilon = (dw/dt)/g$ becomes significant, the dissipation starts to play a prominent role in creating strong energy sinks.

Two options are available in the model for dealing with the problem of semi-staggered grids with the frequencies of short gravity-inertia waves. The first is the selective filtering technique proposed in Janjic (1979). The second is the deaveraging technique proposed by Janjic et al. (1998). The deaveraging is computationally very efficient and requires only a few simple iterations on the hydrostatic pressure tendency. Although the deaveraging is non-dissipative, and therefore physically better founded, the dramatic improvement in the frequencies of the shortest gravity-inertia waves achieved on the semi-staggered grids requires that the time step be significantly reduced, which leads to reduced computational efficiency in the model. Thus, it is not obvious which of the two options should be given preference in practical NWP applications, particularly in the light of the situation shown in Fig. 5.

Concerning the vertical discretization of the basic dynamical variables, quadratic conservative vertical advection is used. In addition to material surface boundary conditions requiring that the total derivative of the vertical coordinate (vertical velocity) be equal to zero at the top and bottom of the model's atmosphere, vertical boundary conditions are needed also for the nonhydrostatic deviation of pressure. It is assumed that the nonhydrostatic pressure deviation vanishes at the top of the atmosphere, while its vertical derivative vanishes at the bottom (Janjic et al., 2001).

The centered conservative schemes used for advection of the basic dynamic variables develop well known problems in case of advection of positive definite scalars with large spatial variation, such as specific humidity, cloud water, or turbulence kinetic energy. For this reason, an upgraded version of the scheme used for advection of passive substances in the NCEP Meso (Eta) model (Janjic, 1997) is applied. The scheme consists of three steps. In the first step, an upstream biased scheme is used to advect the passive substance. In the second step, antifiltering is applied with antifiltering parameters optimized in such a way as to minimize the computational dispersion in sheared flows. Finally, in the third step, forced conservation of the advected quantity is imposed. The scheme appears to be a reasonable compromise between the requirements for accuracy and computational efficiency.

7. TIME DIFFERENCING

The hydrostatic core of the system of nonhydrostatic equations (2.1)-(2.10) is split into the following two subsystems (Janjic, 1979; Janjic et al., 2001; Janjic, 2003)

$$(\frac{\partial \mathbf{v}}{\partial t})_i = -\nabla_\sigma \Phi - \alpha \nabla_\sigma \pi + f\,\mathbf{k}\times\mathbf{v} \qquad (7.1)$$

$$(\frac{\partial T}{\partial t})_i = \frac{\alpha}{c_p}[\mathbf{v}\bullet\nabla_\sigma \pi - \int_0^\sigma \nabla_\sigma \bullet(\mu\mathbf{v})\,d\sigma'] \qquad (7.2)$$

$$(\frac{\partial \mu}{\partial t})_i + \nabla_\sigma \bullet(\mu\mathbf{v}) + \frac{\partial(\mu\dot\sigma)}{\partial\sigma} = 0 \qquad (7.3)$$

$$(\frac{\partial \mathbf{v}}{\partial t})_{ii} = -\mathbf{v}\nabla_\sigma \mathbf{v} - \dot\sigma\frac{\partial \mathbf{v}}{\partial\sigma} \qquad (7.4)$$

$$(\frac{\partial T}{\partial t})_{ii} = -\mathbf{v}\bullet\nabla_\sigma T - \dot\sigma\frac{\partial T}{\partial\sigma} \qquad (7.5)$$

The time derivatives of the two subsystems are denoted by subscripts i and ii, respectively. The systems (7.1)-(7.3) and (7.4)-(7.5) are solved using different time stepping methods. Note that the splitting is not done by automatically separating all the advection terms. Namely, the system with subscripts i includes the advection of pressure in the omega-alpha term of the thermodynamic equation. The contribution of this term compensates for kinetic energy production by the pressure gradient force in the total energy equation. As can be readily verified, due to the presence of this term the system (6.1)–(6.3), conserves energy. The system (6.4)–(6.5) also conserves energy, except for changes due to the redistribution of mass.

An economical forward–backward scheme (Ames, 1969; Gadd, 1974; Janjic and Wiin–Nielsen, 1977; Janjic, 1979) has been used for the system (7.1)–(7.3).

The properties of the scheme used in the model were examined in the case of linearized shallow water equations by Janjic and Wiin–Nielsen (1977) and Janjic (1979). Concerning the contributions of the advection terms (7.4)–(7.5), historically the split, iterative, first–forward–then–(slightly off–) centered time differencing scheme has been applied with time steps twice as long as those used to solve the subsystem (7.1)–(7.3) (Janjic, 1979). This combination has worked very well in the hydrostatic model at synoptic scales (Janjic et al., 1995). However, in the nonhydrostatic model, two-grid-interval noise in time develops with this scheme at high resolution (Janjic, 2003). For this reason, the two–step iterative scheme for horizontal advection has been replaced by the Adams–Bashforth scheme using a short time step. The Adams–Bashforth scheme allows about the same computational efficiency as the two–step, iterative scheme with the longer time steps, and the accuracy is improved. However, somewhat more memory is needed in order to store some of the variables at the third time level, and the physical mode of the Adams–Bashforth scheme is weakly unstable. This instability can be tolerated if the time steps are not too long, or eliminated by a very slight off-centering which preserves the second order accuracy. Note that large ratios between the advection time step and the time step used for the remaining terms of the equations cannot be used in NWP applications. This ratio is restricted to only about 2 on the semi-staggered grids, where longer short steps can be used than those allowed by the CFL criterion on the staggered C grid.

The trapezoidal scheme for Coriolis force terms has been also been recently replaced by the Adams-Bashforth scheme. The reason for this change was the possibility of the trapezoidal scheme overestimating the amplitude of the divergent part of flow (Janjic and Wiin-Nielsen, 1977).

For simplicity, the time differencing has been presented using only the hydrostatic part of the model dynamics. The treatment of the contribution of nonhydrostatic dynamics is more involved, and the details on the time stepping procedures used can be found in Janjic et al. (2001) and Janjic (2003). A novelty in the treatment of the nonhydrostatic terms is that the iterative method for solving the vertical implicit pressure equation discussed in Janjic et al. (2001) has been replaced by a direct solver. This modification has brought a visible further improvement in the computational efficiency of the model. Currently, the passive substance transport remains the single most expensive part of the model dynamics.

8. FIRST EXPERIENCES IN OPERATIONAL APPLICATIONS

Since July 2002, the NMM has been run operationally in NCEP High Resolution windows in six nested domains (Western, Central, Eastern, Alaska, Hawaii, Puerto Rico) shown in Fig. 7. The horizontal resolution is 8 *km* for all domains except for the Alaska domain, where the horizontal resolution is 10 *km*. The model has 60 unequally spaced levels in the vertical.

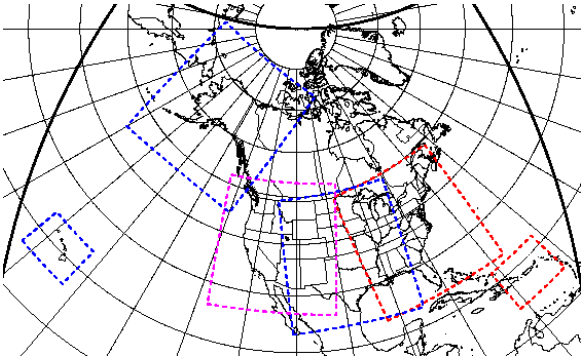

Fig. 7. The six High Resolution Windows: Western, Central, Eastern, Alaska, Hawaii and Puerto Rico.

The model topography is defined as unfiltered gridbox means of 30'' USGS Digital Elevation Model data. The model does not have its own dedicated data assimilation system. The initial and boundary conditions are defined by interpolation of the operational Meso (Eta) model data. The Meso (Eta) model is run with 12 *km* resolution and 60 levels in the vertical.

In the two small domains (Hawaii and Puerto Rico), the model is run twice a day starting from 00 UTC and 12 UTC. In the remaining four domains, the model is run once a day starting from 00 UTC (Alaska), 06 UTC (Western), 12 UTC (Central) and 18 UTC (Eastern). The forecasts are computed up to 48 hours.

The computational efficiency of the model has been very high, substantially higher than the computational efficiency of most established nonhydrostatic models. Moreover, further significant improvement of the computational efficiency of the model is possible. The model has been highly reliable and there have been no failures since operations started.

In terms of performance at synoptic scales, generally the model has been highly competitive with mature high-resolution NWP models, despite the fact that it has been handicapped by inconsistent initial and boundary conditions and a relatively small integration domain. As shown in Fig. 14 (courtesy of Eric Rogers), the most dramatic differences between the Eta model and the NMM can be seen in vertical structures. The

panels in the column on the left are from the 12 *km* Meso (Eta) run, and the panels in the column on the right are from the NMM Eastern domain run. The middle and bottom panels of the two columns represent 12 hour and 15 hour forecast cross sections, respectively, starting at 18 UTC, January 7, 2003. The cross sections are taken along the blue lines in the top panels. The topography is indicated in the top panels by color shading with the contours at 100, 175,

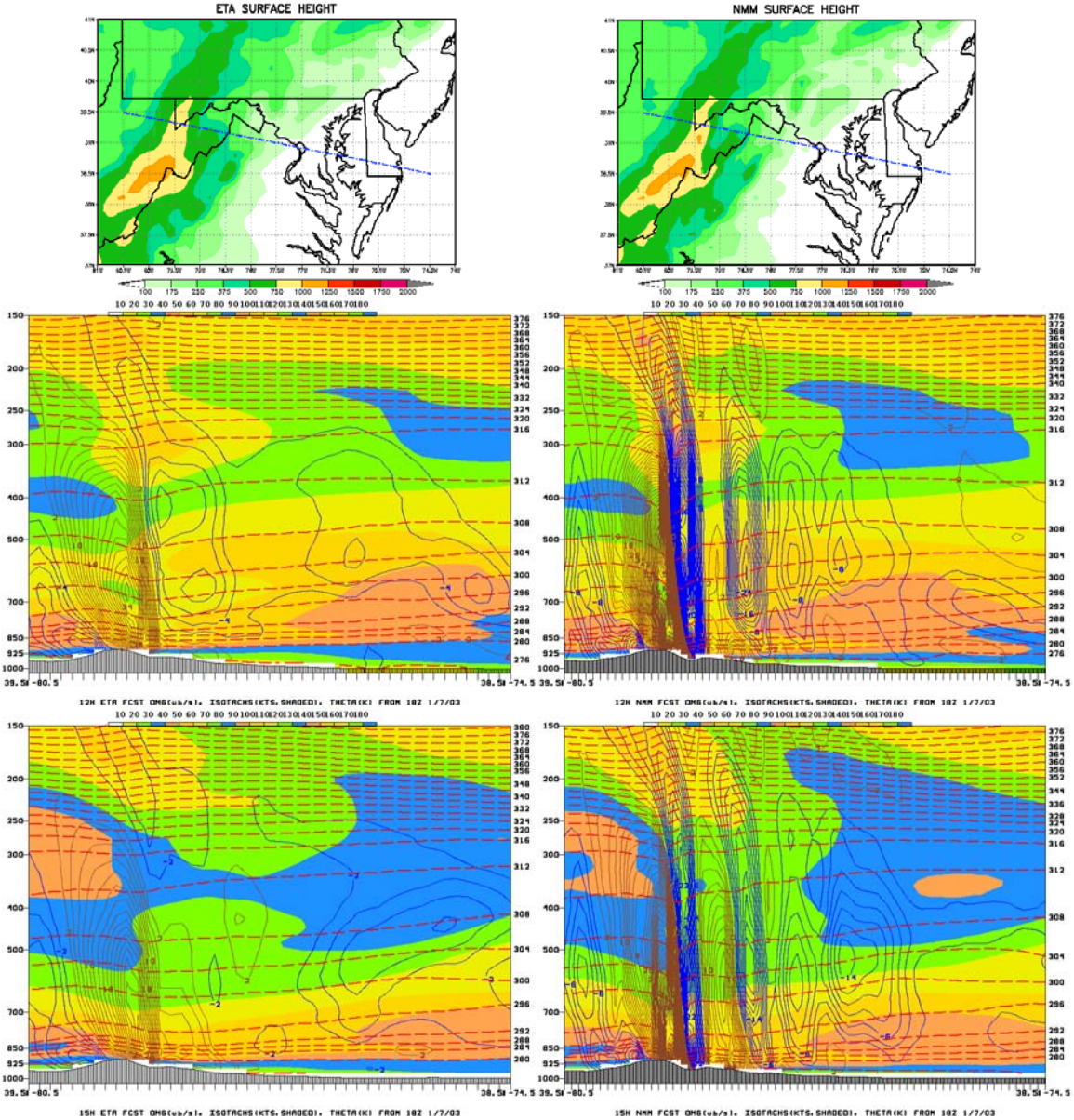

Fig. 14. The 12 *km* Meso (Eta) (left column) and the 8 *km* NMM Eastern Domain (right column) cross sections. The middle and bottom panels are 12 hour and 15 hour forecasts, respectively, starting at 18 UTC, January 7, 2003. The cross sections are taken along the blue lines in the top panels. The topography is indicated in the top panels by color shading with the contours at 100, 175, 250, 375, 500, 750, 1000, 1250 etc. meters, and by the shaded area at the bottom of the cross sections. The blue and brown contour lines are negative (upward) and positive (downward) values of vertical velocity $\omega = dp/dt$, respectively. The contour interval is 0.2 Pa s^{-1}. The dashed red contour lines are potential temperature with a contour interval of 4 degrees. The background color shading in the cross sections represents isotachs with the contour interval of 10 *Knts*. (Courtesy of Eric Rogers)

250, 375, 500, 750, 1000, 1250 etc. meters, and by the shaded area at the bottom of the cross sections. The blue and brown contour lines indicate negative (upward) and positive (downward) values of vertical velocity $\omega = dp/dt$, respectively. The contour interval is 0.2 Pa s^{-1}. Potential temperature is represented by the dashed red contour lines with a contour interval of 4 degrees. The background color shading in the cross sections represents isotachs with a contour interval of 10 *Knts*.

As can be seen from the figure, the vertical motions are much stronger in the NMM than in the Meso (Eta) model. Moreover, the wave length of mountain waves in the NMM is much shorter than in the Meso (Eta) model. Also, the effect of vertical transport of momentum is visible in the bottom panels, particularly in the case of the NMM. In addition to resolution, the representation of mountains and the nonhydrostatic dynamics are believed to have played a role in producing such different results. A more detailed discussion of model performance measures and examples of model forecasts have been/will be presented elsewhere (Black, 2002; Janjic, 2003).

9. SOME RECENT IMPROVEMENTS

9.1 The Convection Scheme

The Betts-Miller-Janjic deep convection scheme (Janjic, 1994, 2001) can be introduced with a simple dimensional formalism. Namely, first the determining parameters are identified as

- Entropy change over time step

$$\Delta S = \sum \frac{c_p \Delta T + L \Delta q}{T} \Delta p \,, \tag{9.1}$$

- Precipitation over time step

$$\Delta P = \sum c_p \Delta T \Delta p \,, \tag{9.2}$$

- Mean temperature of the cloud

$$\overline{T} = \frac{\sum c_p (T + \frac{\Delta T}{2}) \Delta p}{\sum \Delta p} \,. \tag{9.3}$$

Here, p is pressure, T is temperature, q is specific humidity, and the summation is performed from cloud base to cloud top. The other symbols used have their usual meaning.

Then, a nondimensional combination of the determining parameters is defined

$$E = const \frac{\overline{T} \Delta S}{\Delta P} \,. \tag{9.4}$$

The non-dimensional quantity E is called "cloud efficiency." Depending on E, the equilibrium temperature and moisture profiles oscillate between universal heavy convection profiles based on the Betts (1986) profiles, and the moist adiabat (Janjic, 1994). When ΔS and, consequently, E tend to zero, the profiles approach the moist adiabat. In the case of large entropy changes relaxation toward the reference profiles is faster than in the case of more stable stratification closer to the moist adiabat (Janjic, 1994).

Recent upgrades of the deep convection algorithm include iterative computation of cloud efficiency and an iterative search for the cloud top. The latter reduces the number of points with aborted deep convection.

Furthermore, an attempt has been made to improve the transition between the convection and the grid-scale precipitation that depends on resolution. Namely, the entropy change measures the stabilization of the column. Thus, if the threshold for entropy change needed for the onset of the deep convection is increased with increasing resolution, the instabilities that were handled by the parameterization of convection at coarser resolutions will be treated explicitly at higher resolutions.

An example of accumulated 24 hour precipitation for the tropical storm Isabel, obtained using several modifications (including the described modifications of the convection scheme other than changing the threshold for the entropy change), is shown in the upper left panel of Fig 15. The precipitation forecast in the upper right panel illustrates the impact of the increased threshold for the entropy change required for the onset of the deep convection. Finally, the verifying analysis valid on September 19, 2003 at 12Z is shown in the lower panel. The same color code is used for all the forecast and verification plots.

As can be seen from the plots, an already remarkably good forecast has had a significant further improvement by modifying the entropy change criterion, particularly in Pennsylvania. The minute details successfully reproduced by the model in Northern Virginia (next to the border with West Virginia) should be noted as well.

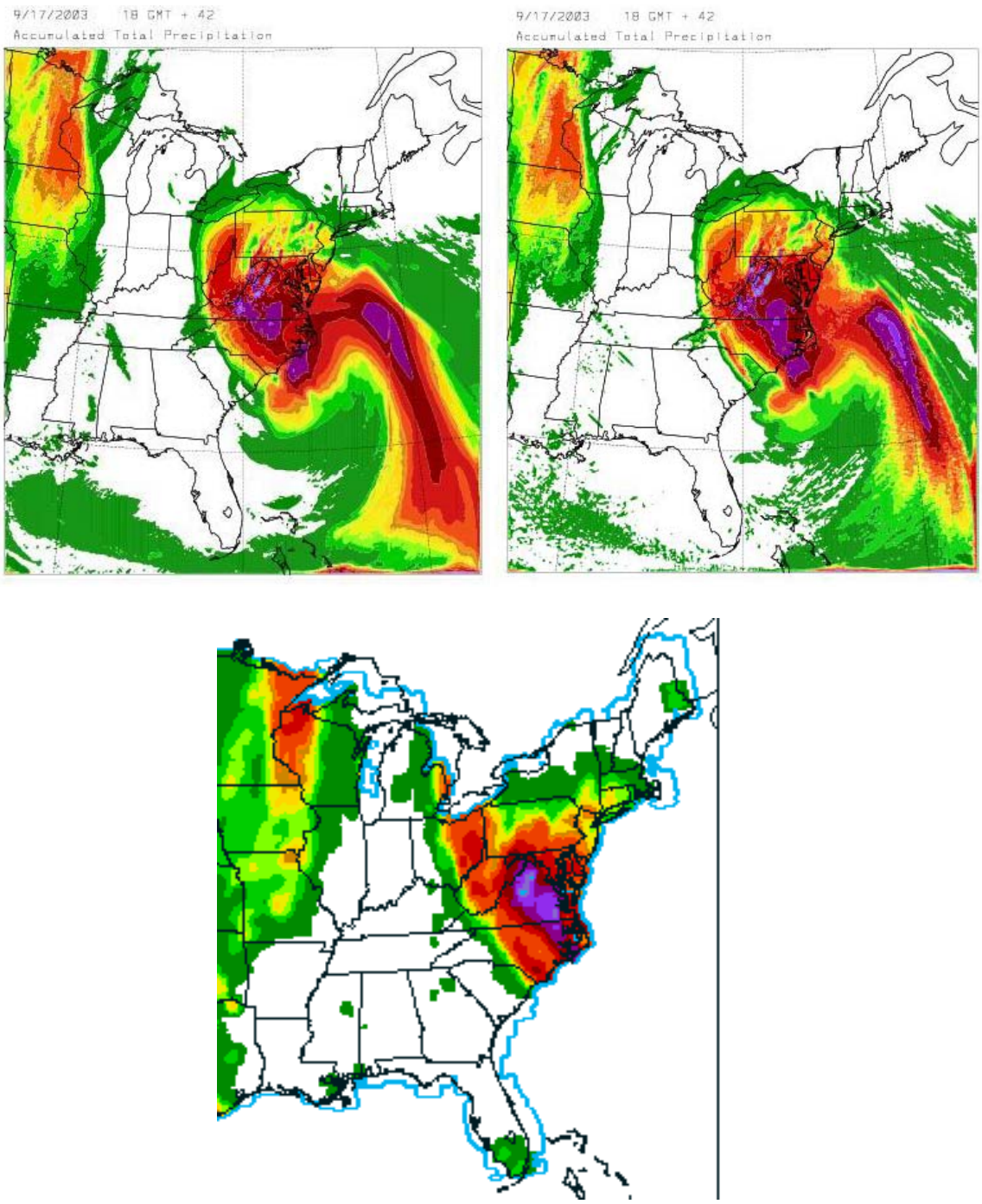

Fig. 15. Accumulated 24 hour precipitation for the tropical storm Isabel without increased entropy change threshold (upper left panel), with increased entropy change threshold (upper right panel), and the verifying analysis valid on September 19, 2003 at 12Z (lower panel).

9.2 Lateral Diffusion on Sloping Surfaces

It has been known for a long time that horizontal diffusion applied in terrain-following coordinates can create spurious instabilities and precipitation by transporting heat and moisture from surrounding valleys to hill tops. In order to cope with this problem, as an ad hoc measure, the lateral diffusion of heat and moisture is switched off if the slope of the coordinate surfaces $\Delta z / \Delta x$ exceeds 0.001.

9.3 Lateral Boundary Conditions

A high positive bias in geopotential height at 500 *hPa* has been observed this summer in the High Resolution and Fire Weather domains with lateral boundaries running through mountainous areas. Inspection of the temperature forecasts did not reveal signs of overheating of model's atmosphere. Since the model conserves the mass exactly, an imbalance of inflow and outflow of mass remained as the main suspect for the problem.

In order to improve the accuracy of mass flux interpolation along the lateral boundaries, the local quadratic interpolation in the vertical was replaced by cubic spline interpolation, and, in addition, the vertical integrals of mass fluxes along the lateral boundaries after the vertical interpolation are required to coincide with those before the interpolation.

These simple modifications have been introduced into the operations starting at the 12Z cycle on October 7, 2003, and resulted in a dramatic improvement of the scores. For example, the mean errors in 500 *hPa* geopotentials in the Central Domain for the Eta and for the NMM are shown in Fig. 16 by the

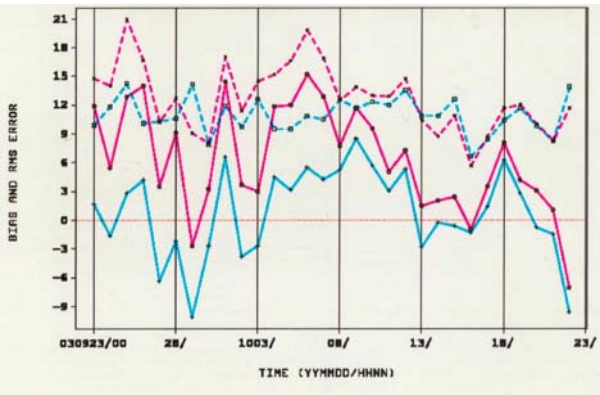

Fig. 16. The mean errors in 500 *hPa* geopotential in the Central Domain for the Eta (solid blue line) and for the NMM (solid pink line) and the RMS errors for the Eta (dashed blue line) and the NMM (dashed pink line).

solid blue and pink lines respectively. The corresponding RMS errors are shown in the figure by dashed blue and pink lines. As can be seen from the plots, the difference in bias errors between the two models has been significantly reduced after the introduction of the modifications, and the NMM has started winning the RMS score in this domain as well.

10. THE OBSERVED MESOSCALE SPECTRUM AND THE NMM NONLINEAR DYNAMICS

Nastrom and Gage (1985) examined measurements made by commercial aircraft and found that one-dimensional kinetic energy spectra along their flight-paths in the lower stratosphere and in the upper troposphere follow the –5/3 slope in the range from several hundred kilometers to several kilometers. As of now, there is no universally accepted explanation of this spectral shape. Several possible explanations have been proposed (e.g. Gage, 1979; Lilly, 1983; Gage and Nastrom, 1986; Tung and Orlando, 2003). They include downscale nonlinear energy cascade and an inverse cascade from smaller to larger scales.

Using two-parameter quasi-geostrophic dynamics, Tung and Orlando (2003) demonstrated that given enough time to reach the statistical equilibrium, the –5/3 spectral range can be generated through a downscale cascade of energy. Similar statistical properties of the spectra were obtained in extended simulations using the GFDL SKYHI model with quite modest horizontal resolution (but still higher than usual for a climate model) (e.g., Hamilton et al., 1999; Kosyik and Hamilton, 2001).

Recently, there have been reports that the –5/3 spectral range has been successfully reproduced in short-range integrations (up to two days) using a high-resolution mesoscale atmospheric model over mountainous areas (communicated by Skamarock). Generally, this should come as no surprise considering that models with much simpler dynamics and coarser resolution have successfully spun-up the –5/3 spectrum (e.g., Hamilton et al., 1999; Kosyik and Hamilton 2001; Tung and Orlando, 2003). However, these mesoscale runs were made on a much shorter time scale than those considered in most previous studies. Namely, the statistical properties of atmospheric spectra are typically investigated in extended integrations (tens or hundreds of days), and the spectra are averaged over long periods (tens or hundreds of days) in order to ensure that statistical equilibrium is reached. The need for extended integrations and long averaging periods arises due to the time scale of the nonlinear cascade.

Despite the time scale problem, in short range runs the model spectrum can perhaps still be close to the

statistical atmospheric spectrum if the initial data are well balanced and do not deviate too much from observed statistics. However, consider the possibility that the initial data are not well balanced, and that they do deviate considerably from the observed atmospheric spectrum in the mesoscale range. This may be, for example, due to the imperfections of the driving model, or to the set-up of the data assimilation system. In addition, the size of the integration domain in mesoscale runs is typically smaller than the size of large-scale atmospheric disturbances that feed the downscale nonlinear cascade. Thus, it appears that physical or spurious sources of energy other than the downscale nonlinear cascade from large-scale motions are needed in order to generate and maintain the –5/3 spectra in mesoscale atmospheric models.

Possible sources that can generate and maintain the –5/3 spectrum in mesoscale models may be (a) physically justified mesoscale forcing, (b) early collapse of the spectrum due to spurious computational nonlinear cascade, (c) other small-scale computational errors such as errors due to the representation of topography, etc. In order to clarify the situation, several tests have been performed using two versions of the NMM, the parallel version on the E grid (WRF-NMM) and the PC version on the B grid (NMM-B). Both versions were designed by applying the same principles in the discretization of the model dynamics and share the same physical package (Janjic et al., 2001; Janjic, 2003).

It should be noted that the WRF-NMM and the NMM-B are well qualified for investigating atmospheric spectra. They conserve energy and enstrophy, which generally improves the accuracy of the nonlinear dynamics. In particular, the energy and enstrophy conservation controls the nonlinear energy cascade and restricts an early spurious energy transfer toward smaller scales by nonlinear interactions. The energy conservation improves the stability of the model and eliminates the need for excessive dissipation (either explicit or built into the finite-difference schemes) that could affect the spectra generated by the model. In addition, WRF-NMM and NMM-B use the hybrid pressure-sigma vertical coordinate, so that (except for errors propagating from below) in the upper troposphere and in the stratosphere they are relatively free of the sigma coordinate errors that are largest at higher altitudes. Finally, explicit formulation of major dissipative processes allows precise “dosage” of dissipation.

The topography used in all tests is defined as grid-box means of the USGS 30’’ global data. Except in ten rows along the lateral boundaries, no smoothing or filtering is applied. The test with the operational set-up of WRF-NMM over the Central Domain, but in the sigma coordinate, generated the –5/3 spectral slope on constant pressure surfaces in the upper troposphere and stratosphere. An example of the spectrum (blue diamonds) obtained at the 300 *hPa* level, and averaged over forecast times from 24 to 36 hours with 3 hour intervals, is shown in Fig. 17. As can be seen from the figure, the model develops the spectrum (blue

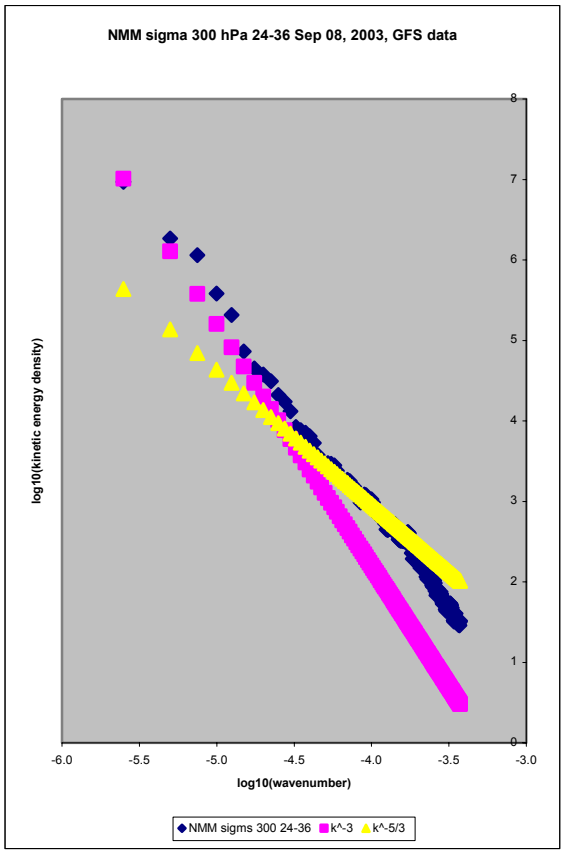

Fig. 17. The WRF-NMM spectrum (blue diamonds) at 300 *hPa* averaged over forecast times from 24 to 36 hours with 3 hour intervals produced with operational set-up in Central Domain, but in the sigma coordinate. The –3 (pink squares) and –5/3 (yellow triangles) slopes are shown for comparison.

diamonds) following the –3 (pink squares) and the –5/3 (yellow triangles) slopes that is in very good agreement with observations.

However, there are problems with interpretation of this result. Namely, when the operational set-up of the WRF-NMM is run in the hybrid coordinate, the spectrum at the small scales remained steeper than the –5/3 slope and approached the –3 slope (not shown). Another reason for concern is that, as can be seen from Fig. 18, the spectrum of the square of unfiltered

topography (blue diamonds) follows the –5/3 law in the mesoscale range. This result, together with the lack of –5/3 range in the hybrid coordinate runs, calls into question the validity of the interpretation of the results obtained in the sigma coordinate over mountainous areas as the model generated Nastrom and Gage (1985) spectra. Namely, the –5/3 spectrum in the upper troposphere and in the stratosphere could be generated by nonlinear cascade of spurious energy due to the sigma coordinate errors. In this case, the computational

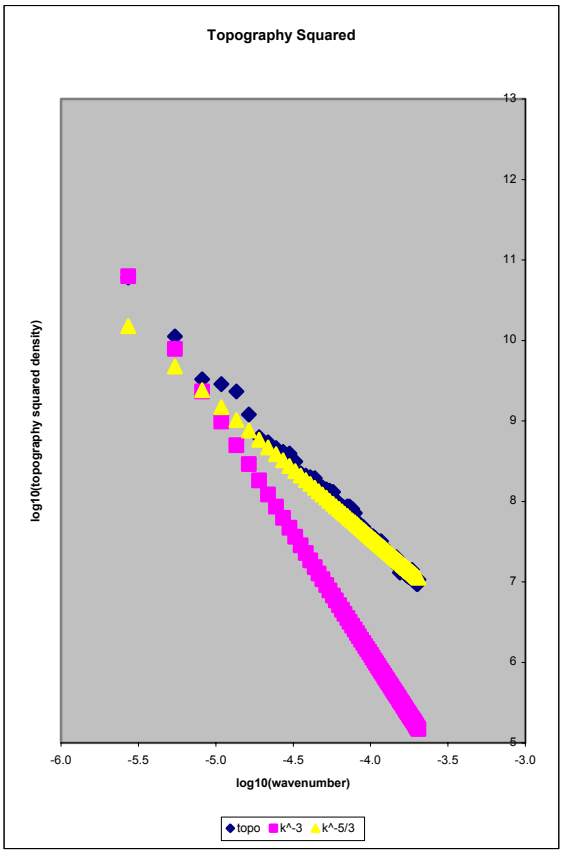

Fig. 18. The spectrum (blue diamonds) of the square of unfiltered topography height in the NMM-B Central Domain with 15 km resolution. The –3 (pink squares) and –5/3 (yellow triangles) slopes are shown for comparison.

noise would be mistaken for the Nastrom and Gage (1985) spectrum. On the positive side, one could argue that the nonlinear dynamics still performed well generating the –5/3 spectrum, although for a wrong reason. However, considering the shape of the mountain spectrum, the –5/3 spectrum observed in model integrations over mountainous areas could be simply a projection of the spectrum of topography, and thus may have nothing to do with nonlinear dynamics.

In order to investigate the possible effects of topography, the NMM-B was run using 15 *km* of horizontal resolution and 32 levels of vertical in a domain same size as the Central Domain, but over the Atlantic Ocean. In this way the possibility of mountains influencing the energy spectrum is eliminated. In addition, in a major deviation from the operational set-up, the lateral diffusion was turned off in order to facilitate and speed-up the accumulation of energy at small scales. However, weak divergence damping was still used.

The evolution of NMM-B spectra at 300 *hPa* over Atlantic Ocean (blue lines) is shown in Fig. 19 at 6 hour intervals (6-24 hours, top to bottom in the left column and 30-48 hours, top to bottom in the right column). The –3 (pink lines) and –5/3 (yellow lines) slopes are shown for comparison. The spectral time average over 36-48 hours is shown in Fig. 20. As can be seen from Fig. 20, by the end of the forecast, the model (blue diamonds) developed the –3 (pink squares) and the –5/3 (yellow triangles) spectral ranges that agree well with observations. However, as can be seen from Fig. 19, it needed 24-36 hours to do so. Note that the sharp drop-off of the spectrum that is usually seen in numerical simulations at the small-scale end of the spectrum is missing here because of very weak dissipation.

The WRF-NMM run in the Eastern Domain in the case of hurricane Isabel (initial data September 17, 18Z, from the Eta data) with 8 *km* resolution and 60 levels, and with no lateral diffusion, showed consistent behavior. The evolution of WRF-NMM spectra (blue lines) at 300 *hPa* in the Eastern Domain is shown in Fig. 21 at 6-hour intervals (6-24 hours, top to bottom in the left column, 30-48 hours, top to bottom in the right column). The –3 (pink lines) and –5/3 (yellow lines) slopes are shown for comparison. The time average over 36-48 hours of the spectra (blue diamonds) is shown in Fig. 22 together with the –3 (pink squares) and –5/3 (yellow triangles) slopes. As can be seen from Fig. 22, by the end of the forecast the WRF-NMM also generated well developed –3 and–5/3 spectral ranges in agreement with the observations. However, as can be seen from Fig. 21, WRF-NMM needed some time to do so, but perhaps somewhat less than in the previous run of NMM-B over the Atlantic Ocean. It may be that the generation of the –5/3 spectrum was aided in this case by a more vigorous downscale nonlinear energy cascade since there was more energy at scales smaller than the integration domain size.

As expected on the basis of theoretical considerations, the presented results demonstrate that the nonlinear dynamics used in the NMM have been successful in reproducing the observed mesoscale

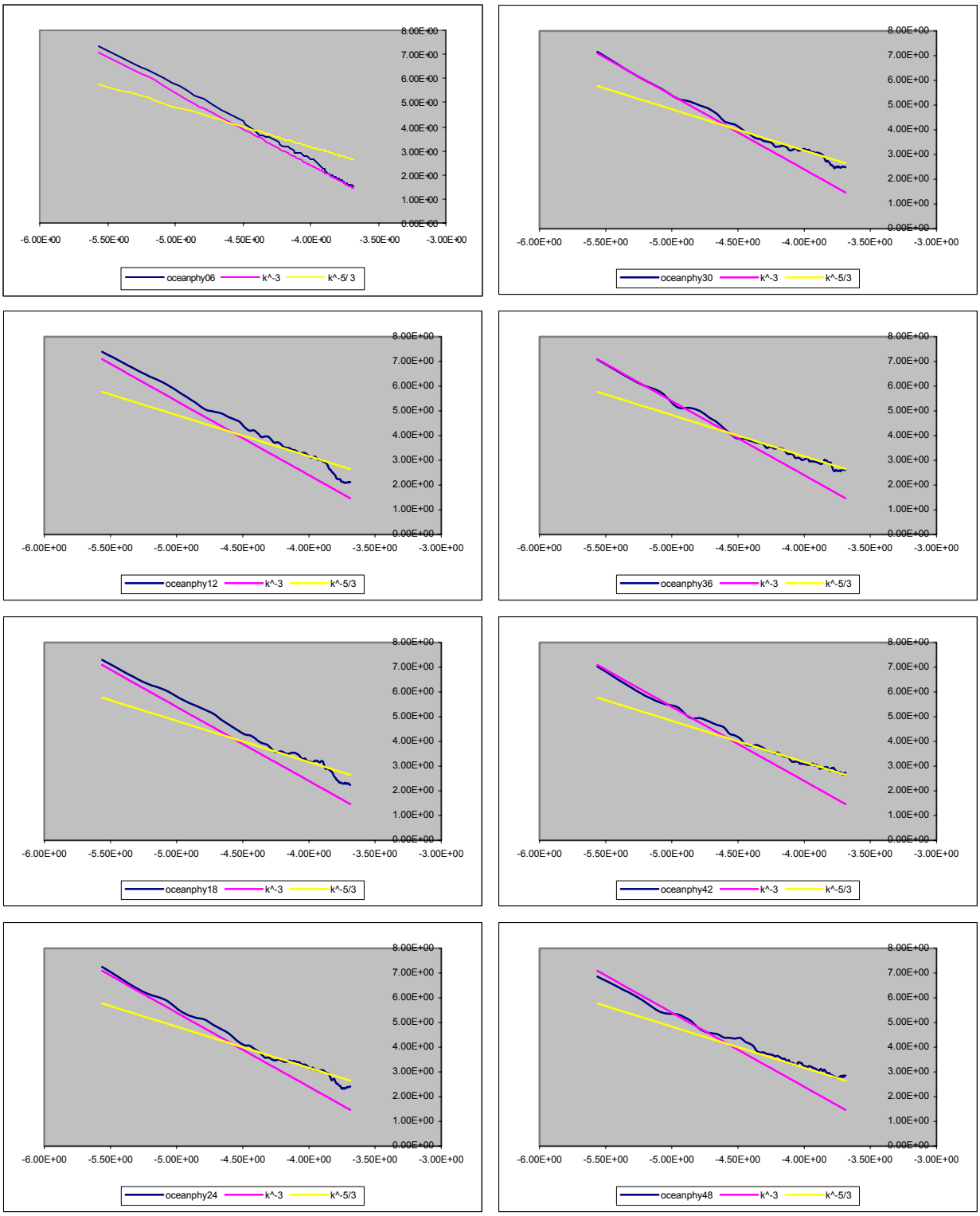

Fig. 19. Time evolution of the NMM-B spectra (blue lines) at 300 *hPa* over Atlantic Ocean. . The –3 (pink lines) and –5/3 (yellow lines) slopes are shown for comparison Run starting from 12 UTC, 09/07/2003, GFS data, 15 *km*, 32 levels resolution. No lateral diffusion, weak mass divergence damping. Plots every 6 hours, top to bottom, 6-24 left column, 30-48 right column.

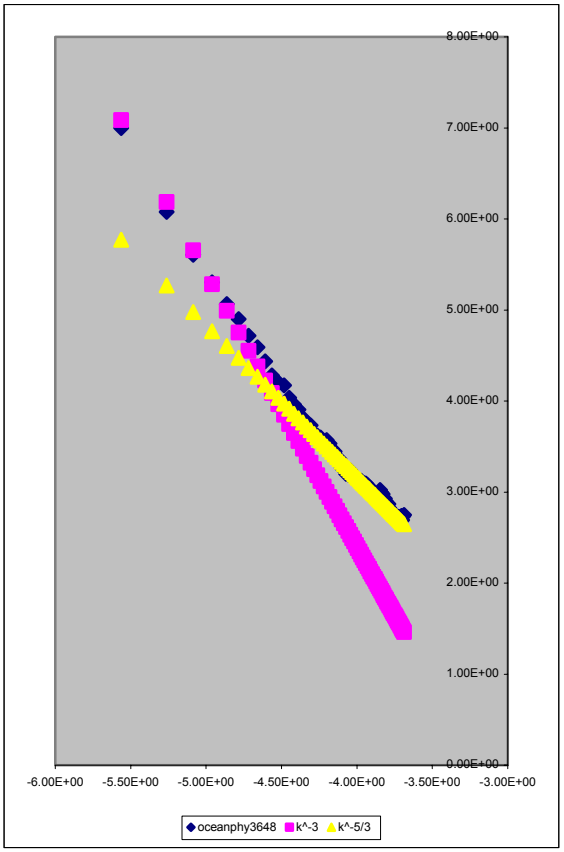

Fig. 20. Time average over 36-48 hours of the NMM-B spectra (blue diamonds) at 300 *hPa* over Atlantic Ocean. The –3 (pink squares) and –5/3 (yellow triangles) slopes are shown for comparison. Run starting from 12 UTC, 09/07/2003, GFS data, 15 *km*, 32 levels resolution. No lateral diffusion, weak mass divergence damping.

atmospheric spectra, even at a rather modest resolution of 15 *km*, and even without forcing by the mountains. Whether the energy at the small-scale part of the spectrum comes from legitimate physical sources, or from computational noise due to model imperfections is another issue that requires further investigation. In other words, there is still no guarantee that the model produced –5/3 spectrum is generated by the same mechanisms as the Nastrom and Gage –5/3 spectrum observed in nature. If it turns out that the model produced spectrum in short-range integrations is physically justified, the shape of the spectrum produced by the model could perhaps be used as guidance for more precise tuning of the model's dissipation parameters.

11. CONCLUSIONS

The NCEP nonhydrostatic meso model (NMM) (Janjic et al., 2001; Janjic, 2003) has been formulated by building on the experience of high resolution hydrostatic numerical weather forecasting. In this way, the favorable features of hydrostatic model formulation are preserved within the valid range of the hydrostatic approximation.

The basic idea applied was to split the system of nonhydrostatic equations into two parts: (a) the part that corresponds basically to the hydrostatic system, except for higher order corrections due to vertical acceleration, and (b) the system of equations that allows the computation of corrections appearing in the first system due to vertical acceleration. This procedure does not require any linearization or additional approximation.

The nonhydrostatic dynamics are introduced through an add–on module. The separation of the nonhydrostatic contributions shows in a transparent way where, how, and to what extent relaxing the hydrostatic approximation affects the familiar hydrostatic equations. The nonhydrostatic module can be turned on and off, so that the same model can be run in both hydrostatic and nonhydrostatic modes. This allows for easy comparison of hydrostatic and nonhydrostatic solutions of an otherwise identical model. This feature also allows the model to be run in the hydrostatic mode at lower resolutions with no extra cost. This is an advantage in the case of models designed for a wide range of horizontal resolutions, and in particular for unified global and regional forecasting systems.

At very high resolutions, a two-dimensional version of the model successfully reproduced the classical nonhydrostatic solutions (Janjic et al., 2001). Although such resolutions will not be affordable in NWP applications in the near future, it was necessary to pass these tests in order to demonstrate the soundness of the formulation.

The extra computational cost due to the nonhydrostatic extension is on the order of 20% of the cost of the hydrostatic dynamics. The relatively low cost of the nonhydrostatic dynamics justifies the application of the nonhydrostatic model even at medium resolutions. Compared to the hydrostatic version of the model, no additional computational boundary conditions at the top have been needed in real data runs at a wide range of horizontal resolutions.

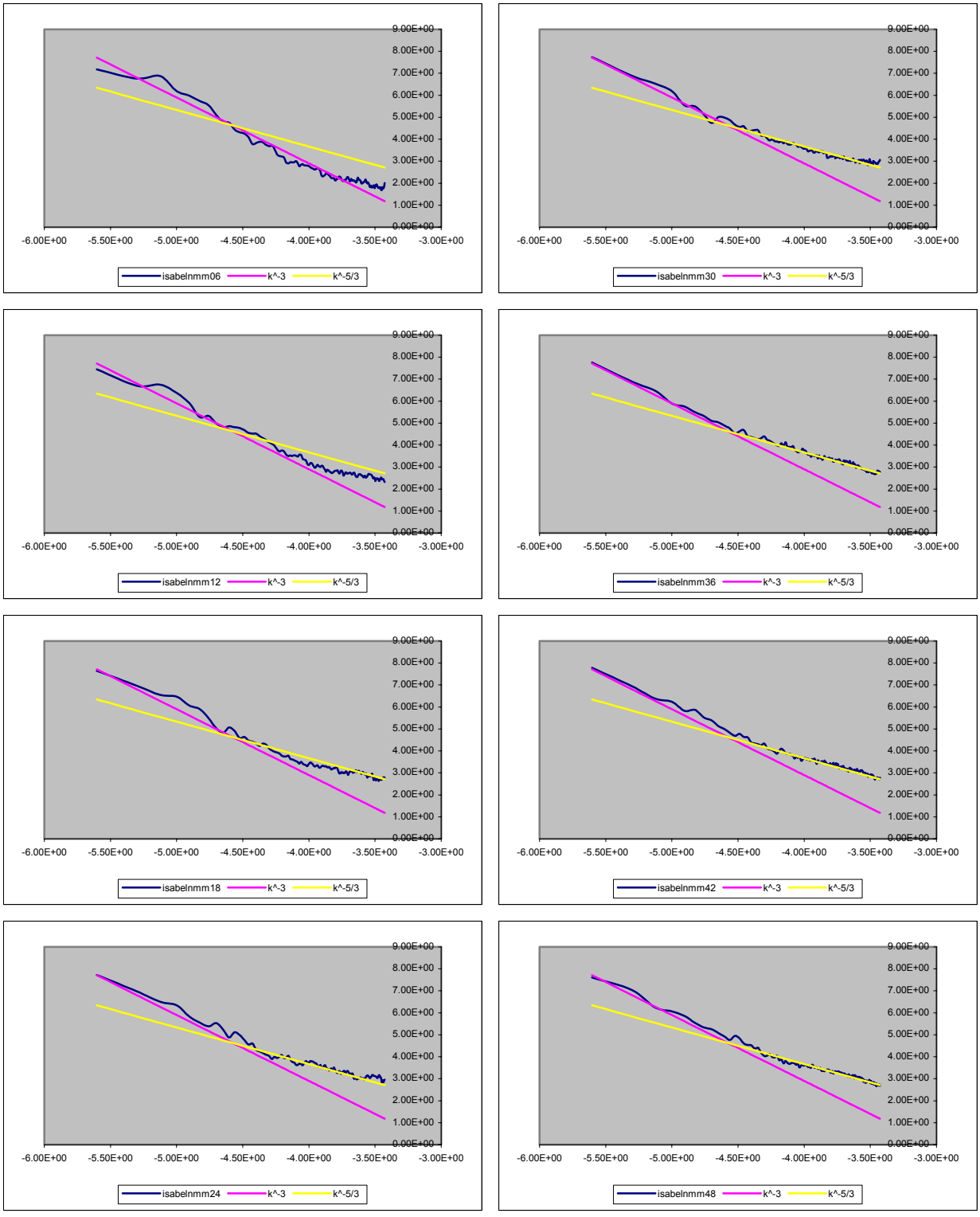

Fig. 21. Time evolution of the WRF-NMM spectra (blue lines) at 300 *hPa* in the Eastern Domain. Run starting from 18 UTC, 09/17/2003 (Isabel), Eta data, 8 *km*, 60 levels resolution. The –3 (pink lines) and –5/3 (yellow lines) slopes are shown for comparison. No lateral diffusion, weak mass divergence damping. Plots every 6 hours, top to bottom, 6-24 left column, 30-48 right column.

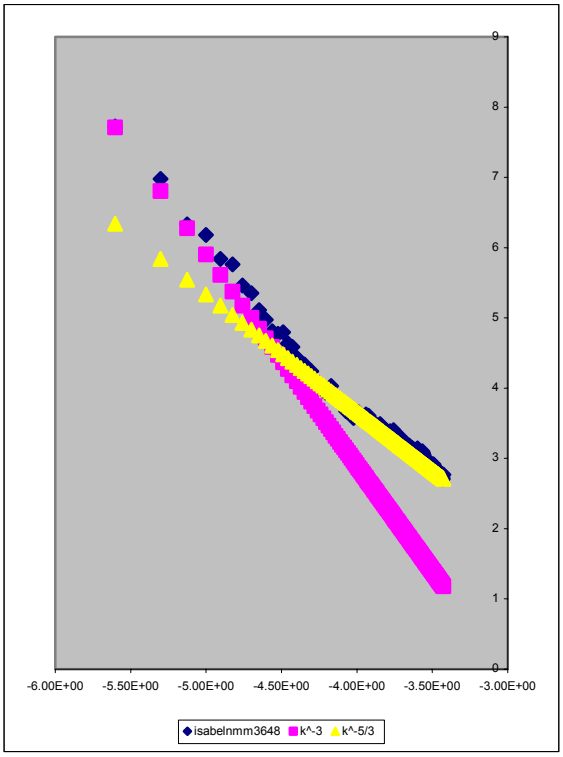

Fig. 22. Time average over 36-48 hours of the WRF-NMM spectra (blue diamonds) at 300 *hPa* in the Eastern Domain. The –3 (pink squares) and –5/3 (yellow triangles) slopes are shown for comparison. Run starting from 18 UTC, 09/17/2003 (Isabel), Eta data, 8 *km*, 60 levels resolution. No lateral diffusion, weak mass divergence damping.

The NMM became operational at NCEP in July of 2002 and has demonstrated remarkable skill (Black et al., 2002). In real data runs, it does not require additional computational boundary conditions at the top.

Despite the application of sophisticated numerical methods, the computational efficiency of the model has been very high, substantially higher than the computational efficiency of most established nonhydrostatic models. Moreover, further significant improvement in the computational efficiency of the model is possible. This will allow for further increases in resolution and the application of more sophisticated physical parameterizations. The model has been highly reliable and there have been no failures since operations started.

In terms of performance at synoptic scales, the model has generally been highly competitive with mature high-resolution NWP models, despite the fact that it has been handicapped by inconsistent initial and boundary conditions, a relatively small integration domain, and almost no retuning of the physical parameterizations. Moreover, it has demonstrated an ability to add value to the forecasts produced by the driving model [the Meso (Eta)].

More significant differences between the NMM and the NCEP hydrostatic high resolution Meso (Eta) model can be seen at smaller scales. The differences are particularly striking in mesoscale vertical structures developed by the two models.

Although the initial results have been very encouraging, further efforts are needed in order to develop the full potential of the model. This applies primarily to retuning the physical parameterizations that are currently tuned for the Eta model. Fast progress in this respect have been hampered by a lack of resources at NCEP that have been further aggravated by problems associated with the migration to new computers.

References

Adcroft, A., C. Hill and J. Marshall, 1997: Representation of topography by shaved cells in a height coordinate ocean model. *Mon. Wea. Rev.*, **125**, 2293–2315.

Arakawa, A. and V. R. Lamb, 1977: Computational design of the basic dynamical processes of the UCLA general circulation model. Methods in Computational Physics, 17, Academic Press, 173-265.

Betts, A.K., 1986: A new convective adjustment scheme. Part I: Observational and theoretical basis. *Q. J.R. Meteorol. Soc.*, **112**, 677-691.

Black, T., E. Rogers, Z. Janjic, H. Chuang, and G. DiMego, 2002: Forecast guidance from NCEP's high resolution nonhydrostatic mesoscale model. 15th Conf. on NWP, San Antonio, TX, Amer. Meteor. Soc., J23-J24.

Bryan, K., 1969: A numerical method for the study of the circulation of the World Ocean. *J. Comp. Phys*, **4**, 347-376.

Chen, F., Z. Janjic and K. Mitchell, 1997: Impact of atmospheric surface–layer parameterization in the new land–surface scheme of the NCEP mesoscale Eta model. *Boundary–Layer Meteorology* **48**, 391–421.

Gage, K.S., 1979: Evidence far a $k^{-5/3}$ Law Inertial Range in Mesoscale Two-Dimensional Turbulence. *J. Atmos. Sci.* **36**, 1950–1954.

Gage, K.S., Nastrom, G.D.. 1986: Theoretical Interpretation of Atmospheric Wavenumber Spectra of Wind and Temperature Observed by Commercial Aircraft During GASP. *J. Atmos. Sci*, **43**, 729–740.

Gallus W. A., Jr., 2000: The Impact of Step Orography on Flow in the Eta Model: Two Contrasting Examples. *Wea. and Forecasting*, 15, 630–639.

Gallus W. A., Jr. and J. B. Klemp, 2000: Behavior of Flow over Step Orography. *Mon. Wea. Rev.,* **128**, 1153–1164.

Gallus, W.A. and M. Rancic, 1996: A non-hydrostatic version of the NMC's regional Eta model. *Q. J.R. Meteorol. Soc.*, **122**, 495-513.

Gavrilov, M. B., 2002: Comments on "A More Extensive Investigation of the Use of Ensemble Forecasts for Dispersion Model Evaluation". *J. Appl. Meteorol.,* **41**, 899.

Gavrilov, M. B. and Z. I. Janjic, 1989: Computed rotational energy spectra of two energy and enstrophy conserving schemes on semi-staggered grids. *Meteorol. Atmos. Phys.,* **41**, 1-4.

Hamilton, Kevin, Wilson, R. John, Hemler, Richard S., 1999: Middle Atmosphere Simulated with High Vertical and Horizontal Resolution Versions of a GCM: Improvements in the Cold Pole Bias and Generation of a QBO-like Oscillation in the Tropics. *J. Atmos. Sci*, **56**, 3829–3846.

Janjic, Z. I., 1977: Pressure gradient force and advection scheme used for forecasting with steep and small scale topography. *Contrib. Atmos. Phys.*, **50**, 186–199.

_____, 1979: Forward–backward scheme modified to prevent two–grid–interval noise and its application in sigma coordinate models. *Contrib. Atmos. Phys.*, **52**, 69–84.

_____, 1984: Non–linear advection schemes and energy cascade on semi–staggered grids. *Mon. Wea. Rev.*, **112**, 1234–1245.

_____, 1990: The step–mountain coordinate: physical package. *Mon. Wea. Rev.*, **118**, 1429–1443.

_____, 1994: The step–mountain eta coordinate model: further developments of the convection, viscous sublayer and turbulence closure schemes. *Mon. Wea. Rev.*, **122**, 927–945.

_____, 1996a: The Mellor–Yamada level 2.5 scheme in the NCEP Eta model. 11th Conf. on NWP, Norfolk, VA, Amer. Meteor. Soc., 333–334.

_____, 1996b: The surface layer in the NCEP Eta model. 11th Conf. on NWP, Norfolk, VA, Amer. Meteor. Soc., 354–355.

_____, 1997: Advection scheme for passive substances in the NCEP Eta model. Research Activities in Atmospheric and Oceanic Modelling, WMO, Geneva, CAS/JSC WGNE, 3.14.

_____, 2000: Comments on "Development and Evaluation of a Convection Scheme for Use in Climate Models. *J. Atmos. Sci.*, **57**, p. 3686

_____, 2002: Nonsingular Implementation of the Mellor-Yamada Level 2.5 Scheme in the NCEP Meso model. NCEP Office Note No. 437, 61 pp.

_____, 2003: A Nonhydrostatic Model Based on a New Approach. *Meteorol. Atmos. Phys.*, **82**, 271-285.

Janjic, Z. and A. Wiin–Nielsen, 1977: On geostrophic adjustment and numerical procedures in a rotating fluid. *J. Atmos. Sci.*, **34**, 297–310.

Janjic, Z. I. and F. Mesinger, 1984: Finite-difference methods for the shallow water equations on various horizontal grids. *Numerical Methods for Weather Prediction,* Vol. 1, Seminar, ECMWF, 1983, Reading, U.K., 29-101, Shinfield Park, Reading, Berkshire RG2 9AX, U.K.

Janjic, Z. I. and F. Mesinger, 1989: Response to small-scale forcing on two staggered grids used in finite-difference models of the atmosphere. *Quarterly Journal of the Royal Meteorological Society,* Vol. **115**, 1167-1176.

Janjic, Z. I., F. Mesinger and T. L. Black, 1995: The pressure advection term and additive splitting in split-explicit models. *Quarterly Journal of the Royal Meteorological Society,* **121**, 524, 953-957.

Janjic, Z. I., J. P. Gerrity, Jr. and S. Nickovic, 2001: An Alternative Approach to Nonhydrostatic Modeling. *Mon. Wea. Rev.*, **129**, 1164-1178.

Janjic, Z. I., and G. DiMego, 2001: Effects of Mountain Representation and Nonhydrostatic Dynamics in a Case of Orographic Precipitation. Symposium on Precipitation Extremes: Prediction, Impacts and Responses. 81st Annual Meeting of the Amer. Meteor. Soc., January 14-19, 2001, Albuquerque, NM, AMS, Boston, MA, 24-28.

Koshyk, John N., Hamilton, Kevin, 2001: The Horizontal Kinetic Energy Spectrum and Spectral Budget Simulated by a High-Resolution Troposphere–Stratosphere–Mesosphere GCM. *J. Atmos. Sci,* **58**, 329–348.

Lilly, D.K., 1983: Stratified Turbulence and the Mesoscale Variability of the Atmosphere. *J. Atmos. Sci*, **40**, 749–761.

Mesinger, F., Z.I. Janjic, S. Nickovic, D. Gavrilov and D.G. Deaven, 1988: The step–mountain coordinate: model description and performance for cases of Alpine lee cyclogenesis and for a case of an Appalachian redevelopment. *Mon. Wea. Rev.*, **116**, 1493–1518.

Nastrom, G.D., Gage, K.S., 1985: A Climatology of Atmospheric Wavenumber Spectra of Wind and Temperature Observed by Commercial Aircraft. *J. Atmos. Sci*, **42**, 950–960.

Phillips, N.A., 1957: A coordinate system having some special advantages for numerical forecasting. *J. Meteor.*, **14**, 184-185.

Simmons, A. J., and D. M. Burridge, 1981: An energy and angular-momentum conserving vertical finite-difference scheme and hybrid vertical coordinates. *Mon. Wea. Rev.*, **109**, 758-766.

Steppeler, Jürgen, Heinz-Werner Bitzer, Maud Minotte, Luca Bonaventura, 2002: Nonhydrostatic Atmospheric Modeling using a *z*-Coordinate Representation. *Mon. Wea. Rev.*, **130**, 2143–2149.

Straka, J.M., R.B. Wilhelmson, L.J. Wicker, J.R. Anderson and K.K. Droegemeier, 1993: Numerical solutions of a non-linear density current: a benchmark solution and comparisons. *Intl. J. Numerical Methods in Fluids*, **17**, 1-22.

Tung, Ka Kit, Orlando, Wendell Welch, 2003: The k^{-3} and $k^{-5/3}$ Energy Spectrum of Atmospheric Turbulence: Quasigeostrophic Two-Level Model Simulation. *J. Atmos. Sci*, **60**, 824–835.